Check for updates

Band-bending induced passivation: high performance and stable perovskite solar cells using a perhydropoly(silazane) precursor†

Hiroyuki Kanda, [ID] [a] Naoyuki Shibayama, [ID] [b] Aron Joel Huckaba, [ID] [a] Yonghui Lee, [ID] [a] Sanghyun Paek, [ID] [a] Nadja Klipfel, [ID] [a] Cristina Roldán-Carmona, [a] Valentin Ianis Emmanuel Queloz, [ID] [a] Giulia Grancini, [ID] [a] Yi Zhang, [ID] [a] Mousa Abuhelaiqa, [ID] [a] Kyung Taek Cho, [ID] [a] Mo Li, [ID] [cd] Mounir Driss Mensi, [f] Sachin Kinge [e] and Mohammad Khaja Nazeeruddin [ID] *[a]

Surface passivation of the perovskite photo absorber is a key factor to improve the photovoltaic performance. So far robust passivation strategies have not yet been revealed. Here, we demonstrate a successful passivation strategy which controls the Fermi-level of the perovskite surface by improving the surface states. Such Fermi-level control caused band-bending between the surface and bulk of the perovskite, which enhanced the hole-extraction from the absorber bulk to the HTM side. As an added benefit, the inorganic passivation layer improved the device light stability. By depositing a thick protection layer on the complete device, a remarkable waterproofing effect was obtained. As a result, an enhancement of V_{OC} and the conversion efficiency from 20.5% to 22.1% was achieved. We revealed these passivation mechanisms and used perhydropoly(silazane) (PHPS) derived silica to control the perovskite surface states.

Broader context

Perovskite solar cells are promising efficient photovoltaic devices and have attracted attention in the research community. A significant emerging point towards high efficiency is passivation technology for perovskite semiconductors. Here, we demonstrate a promising passivation strategy which controls the Fermi-level of the perovskite surface by using a novel inorganic precursor of perhydropoly(silazane). We demonstrated the usefulness of band bending against the depth direction for the first time to the best of our knowledge. It could successfully control the band-bending of the perovskite semiconductor, which led to an improvement of the open circuit voltage and the conversion efficiency from 20.5% to 22.1%. As an added benefit, the inorganic layer had excellent light stability and was waterproof.

Introduction

Investigations into hybrid inorganic–organic perovskite solar cells[1–5] have increased considerably since the first report,[6–9]

[a] Group for Molecular Engineering of Functional Materials, École Polytechnique Fédérale de Lausanne, Valais Wallis, CH-1951 Sion, Switzerland.
E-mail: mdkhaja.nazeeruddin@epfl.ch
[b] Department of General Systems Studies, Graduate School of Arts and Sciences, The University of Tokyo, 3-8-1 Komaba, Meguro-ku, Tokyo 153-8902, Japan
[c] Laboratory of Materials for Renewable Energy, École Polytechnique Fédérale de Lausanne, Valais Wallis, CH-1951 Sion, Switzerland
[d] Swiss Federal Laboratories for Materials Science and Technology, CH-8600 Dübendorf, Switzerland
[e] Toyota Motor Corporation, Toyota Motor Technical Centre, Advanced Technology Div., Hoge Wei 33, B-1930 Zaventum, Belgium
[f] Institute of Chemical Sciences and Engineering, École Polytechnique Fédérale de Lausanne, Valais Wallis, CH-1951 Sion, Switzerland
† Electronic supplementary information (ESI) available. See DOI: 10.1039/c9ee02028d

and device efficiencies have now reached 25.2%.[10] Metal halide perovskite semiconductors have several significant characteristics of optoelectronic properties, such as a large absorption coefficient,[11,12] long charge carrier diffusion length,[13–16] and easily tuneable bandgap.[17–19] These unique semiconductor characteristics could allow efficiency values to approach the Shockley–Queisser limit.[20–22] To further improve the photovoltaic performance beyond the current state of the art, passivation strategies are still needed.

To yield surface passivation in perovskite solar cells, passivation materials such as molybdenum tris(dithiolene) complex,[23] poly(methyl methacrylate) (PMMA),[24] poly(4-vinylpyridine) (PVP),[25,26] phenylethylammonium iodide (PEAI),[27] *n*-hexyl trimethyl ammonium bromide (HTAB),[28] and chloride passivation[29–31] have been used. However, it is still not thoroughly investigated why the passivation layer improves the carrier dynamics in perovskite devices. Thus, a more in-depth understanding of

passivation design strategies needs to be gained to improve further perovskite solar cell efficiencies.

Band-bending is the shifting of the energy band structure caused by differences in the Fermi-level. The main principle underlying band-bending inside a semiconductor is a local imbalance in the space charge.[32] Such band-bending could influence the carrier dynamics at the semiconductor surface.[33–36] Therefore, passivation induced by band-bending can be expected to reduce carrier recombination.

In this study, we demonstrate that band-bending induced passivation can have a beneficial effect on the photovoltaic performance of perovskite solar cells. The influence of the passivation layer on the band structure was investigated by varying the precursor concentration. Herein, we propose a novel passivation concept of band-bending passivation. As an added benefit, the inorganic passivation layer improved the device stability and added remarkable waterproof protection. The experimental results provide a way towards the implementation of a passivation design strategy for perovskite solar cells.

Results and discussion

Material characteristics

Perhydropoly(silazane) (PHPS) is a saturated inorganic polymer consisting of alternating nitrogen–silicon bonds, see Fig. 1a. The reaction of PHPS with oxygen or water generates amorphous silicon dioxide at room temperature (Fig. 1b). The water molecules cause the Si–N bond to be cleaved. In this reaction, PHPS ($R_3Si–NH–SiR_3$) changes to $R_3Si–NH_2$ and $HO–SiR_3$, which can react further to form a Si–O–Si linkage, while ammonia gas is generated at the same time.[37] The amino groups of PHPS may interact with the perovskite surface, which affects the energy band structure on the surface of the perovskite layer. Therefore, it is expected to function as an inorganic passivation layer which modify the surface of the perovsktie layer.

To confirm the presence of the PHPS-derived passivation materials, X-ray photoelectron spectroscopy (XPS) measurements were performed (Fig. 2). After depositing PHPS on a perovskite film, the binding energies of the characteristic Si 2p, O 1s, and

N 1s peaks were measured. The PHPS solution concentration was varied in the range of 0.01–0.2 vol%, and a perovskite sample without PHPS deposition was also analyzed under the same conditions as a reference. In the Si 2p spectra (Fig. 2a), the peak intensity of Si 2p increased with increasing PHPS concentration. The observed Si 2p signal (Fig. 2a) consists of two contributions, which were identified as Si^{4+} (103.3 eV) and Si–O–N (102.5 eV).[38,39] At a low concentration (0.01 vol%), the component of the Si^{4+} peak was predominant, while the proportion of the Si–O–N component increased with increasing PHPS concentration. In the O 1s spectra (Fig. 2b), a peak was identified as the Si–O bond (532.8 eV).[38] We reasoned that PHPS oxidation in ambient air led to Si–O bond formation. In the N 1s spectrum (Fig. 2c), signals corresponding to N–C (400.2 eV) and Si–O–N (398.4 eV) were correlated to the perovskite and silicon oxynitride, respectively.[40,41] These results confirmed the presence of a PHPS derived material on the perovskite surface, which was identified as silicon oxide and silicon oxynitride, forming a thin layer not detectable in the cross-sectional scanning electron microscope (SEM) image (Fig. S1, ESI†). Furthermore, at low PHPS concentration, we could only detect silicon dioxide, while using higher PHPS concentrations yielded silicon dioxide/silicon oxynitride composites, probably due to the incomplete reaction of the PHPS precursor. It is worth noting here that we also observed an apparent effect on the perovskite signals after depositing the passivation layer (Fig. S2, ESI†). As observed in the figure, a clear shift in the Pb 4f binding energy takes place with an increase in the silicon oxide signal (Si–O), while a shift in the I 3d peak occurs simultaneously with the appearance of the silicon oxynitride peak (Si–O–N). These results suggest a strong change in the electronic state around the perovskite surface atoms, which is due to the interaction of Pb/SiOx or I/SiON, respectively.

To determine if the passivation layer affected the perovskite crystallinity and crystallite orientation, we analyzed the perovskite with and without PHPS treatment by two-dimensional wide-angle X-ray scattering (2D-WAXS) (Fig. 3). The reciprocal lattice mapping data indicated a random crystallite orientation for samples with and without the passivation layer as shown in Fig. 3a and b, respectively. Both perovskite layers exhibited an
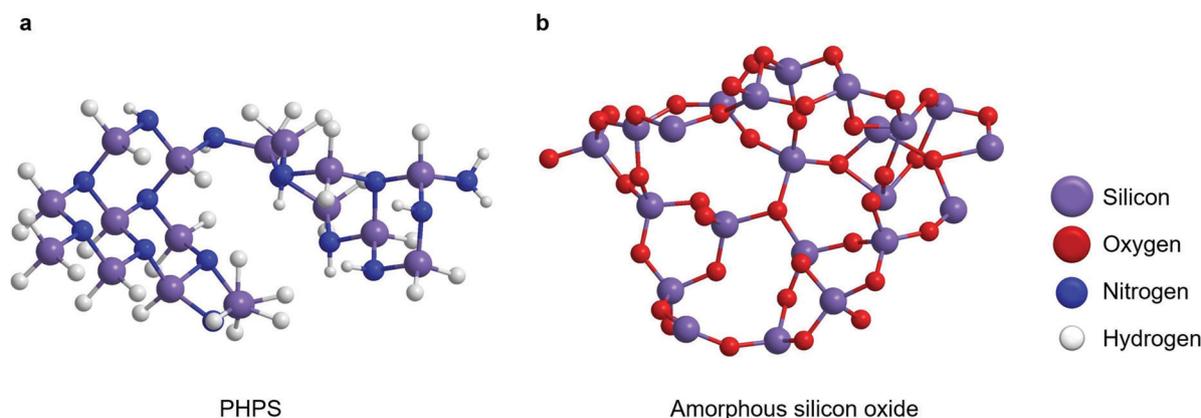
Fig. 1 Representative chemical structures. (a) Perhydropoly(silazane) (PHPS). (b) Amorphous silicon oxide.
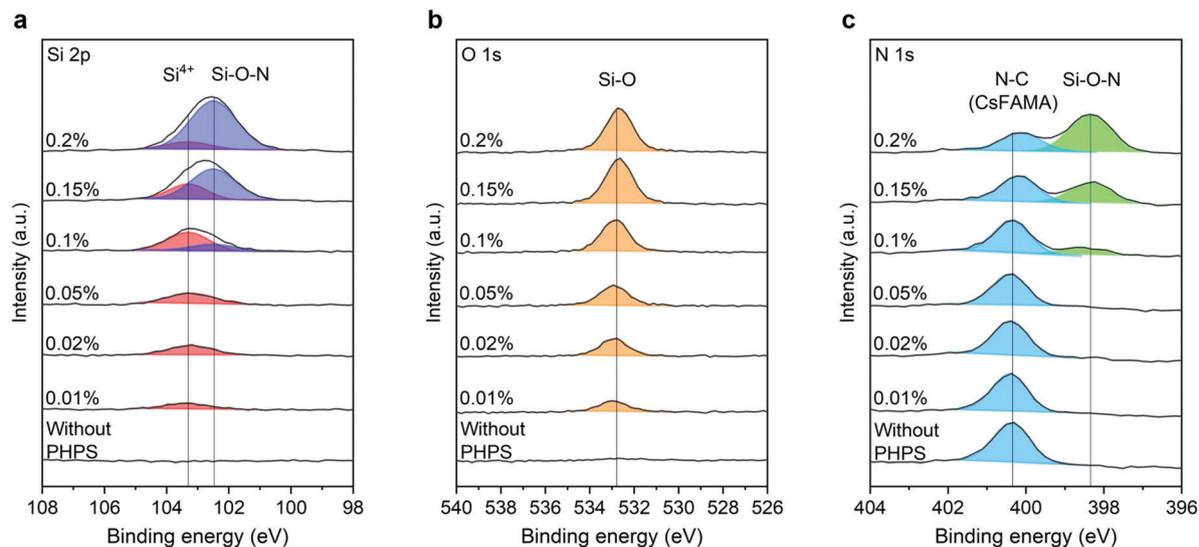
Fig. 2 Material characteristics for the passivation layer. XPS spectra and fitting results of passivation materials on the perovskite layer of (a) Si 2p, (b) O 1s, and (c) N 1s as a function of PHPS concentration.
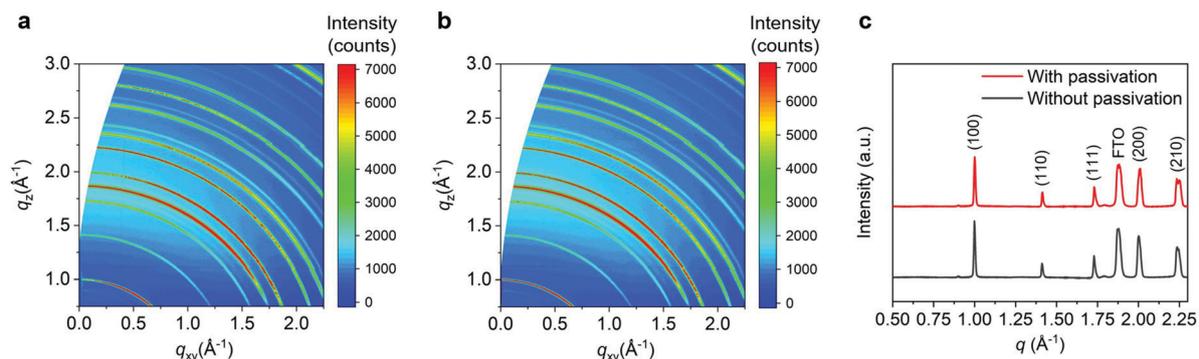
Fig. 3 Crystallinity of the perovskite layer with and without passivation. 2D-WAXS patterns of the perovskite layer (a) with and (b) without passivation. (c) Azimuthally integrated intensity profiles from 2D-WAXS data with and without passivation. The PHPS concentration is 0.02 vol%.

identical cubic structure, which was confirmed through analyzing the azimuthally integrated intensity profiles of 2D-WAXS at the 100, 110, 111, 200, and 210 reflections (Fig. 3c).[42–44] The average perovskite crystal size without PHPS treatment was 300 nm, which was not changed with PHPS treatment (Fig. S3, ESI†). It could, therefore, be confirmed that the passivation layer did not affect the perovskite crystal orientation and structure. Furthermore, no silicon oxide reflection was observed, probably due to the amorphous state of the material.

Photovoltaic performance

We further investigated the influence of the passivation layer on the device efficiency (Fig. 4). Fig. 4a shows the I–V curve for the champion cell with passivation compared to the reference sample without the passivation process. By applying the passivation layer, the open circuit voltage (V_{OC}) was increased from 1.072 V up to 1.135 V (Fig. 4a), which led to a photoconversion efficiency of 22.13% and superior photovoltaic properties (Fig. S4 and S5, ESI†). The certified data show 19.91% in the forward scan, 21.73% in the reverse scan, and 20.82% as an average of

these efficiencies (Fig. S6, ESI†). Fig. 4b shows the V_{OC} distribution as a function of the PHPS concentration. The average V_{OC} value was increased to 1.117 V from 1.061 V without PHPS passivation when depositing a 0.02 vol% solution of PHPS. With increasing PHPS concentration (from 0.01 to 0.2%), the average V_{OC} increased up to 1.135 V for 0.2 vol% PHPS. V_{OC} did not improve using a 0.3% PHPS concentration and the J_{SC}, FF, and efficiency were decreased significantly (Fig. S4, ESI†). The reason for this could be that the passivation layer was too thick to allow easy flow of current. The average series resistance was increased from 10 Ω at 0.02% to 55 Ω at 0.3%, which is consistent with the decrease of the photovoltaic performance. Overall, these results confirm the beneficial effect of PHPS-derived passivation on V_{OC}, and call for deeper investigations.

To understand in more detail why V_{OC} was improved, steady-state PL spectra and PL decay measurements were performed at varied PHPS concentration. Detailed parameters for the PL decay measurements are shown in Table S1 (ESI†). Results obtained for glass/perovskite/passivation layer samples with varying PHPS concentration are shown in Fig. 5a and Fig. S7
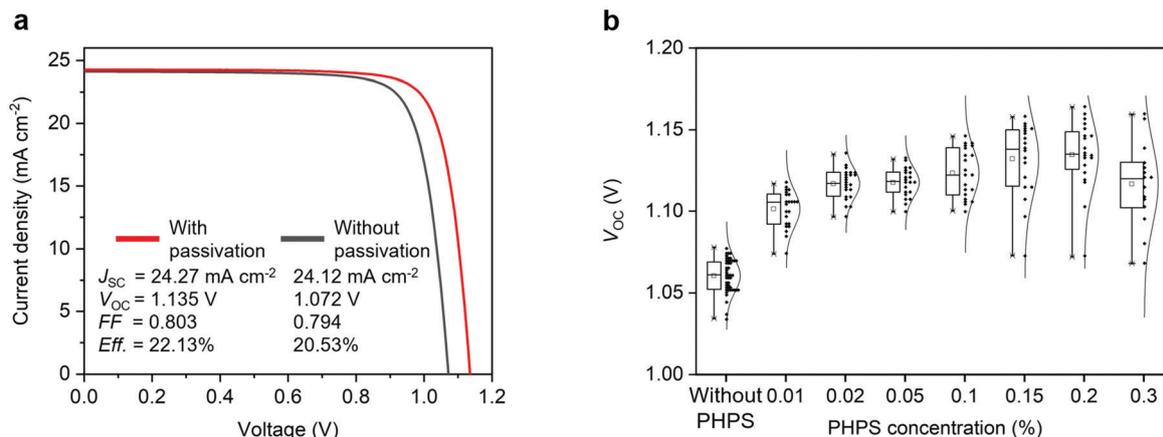
Fig. 4 Photovoltaic performance. (a) $I-V$ curves and photovoltaic properties of the best perovskite solar cell with (PHPS concentration 0.02 vol%) and without passivation. (b) V_{OC} distribution as a function of PHPS concentration.

(ESI†), respectively. Note that the perovskite thickness is the same for all the samples. The intensity of the observed emission peak close to 800 nm increased with increasing PHPS concentration on the perovskite layer compared to the reference sample without passivation, which suggests that the passivation layer reduces the nonradiative pathways. This is consistent with the enhanced emission lifetime shown in Fig. S7 (ESI†) and in correspondence with what has been reported before for passivation with PMMA, PVP, PEAI, and choline chloride.[24,25,27,29] When band-bending was generated on the semiconductor surface, to be explained in detail later, bulk recombination could be dominant rather than surface recombination because there is no electron–hole pair at the surface (Fig. S8, ESI†).[32,45,46] This could be the reason why band-bending reduces the non-radiative pathways (Fig. 5a).

Glass/perovskite/passivation layer/spiro-OMeTAD samples were also prepared to elucidate the hole-transportation at the perovskite/passivation layer/HTM interface (Fig. 5b, Fig. S9 and S10, ESI†). Regarding the steady-state PL spectra (Fig. S9, ESI†), the signal corresponding to films with PHPS (0.02%) was quenched more than samples without PHPS. This reason could be that PHPS can quench emission due to the hole extraction from the perovskite to the HTM side. However, when the PHPS concentration was increased to 0.2%, the PL intensity was increased. We reasoned that the passivation layer was too thick to allow hole transfer. These results are consistent with the following PL decay result (Fig. 5b). For concentrations up to 0.1%, the PL dynamics are increased when compared to the reference sample, indicating that upon the addition of the passivation layer a new decay channel is opened. This can be related to hole transfer enhancement from the perovskite to the HTM through the passivation layer. For concentrations beyond 0.1%, however, the dynamics are slowed down possibly indicating that hole transfer is prevented due to the enhanced thickness of the passivation layer. Indeed, as Wolff et al.[47] have demonstrated, upon inserting an inert interfacial layer, the PL decay is slowed down due to reduced back electron–hole recombination. This phenomenon could explain our observations of the PL decay for PHPS > 0.1%. To understand why the PL decay was slowed down, we measured the series resistance as a function of the PHPS concentration. We found that the series resistance increases up to 55 Ω (at 0.3 vol%) from 10 Ω (at 0.02 vol%) (Fig. S11, ESI†), and the FF decreases to 0.678 (at 0.3 vol%) from 0.799 (at 0.02 vol%). This indicates that hole transfer is hampered at increased PHPS concentration. Also, the perovskite solar cell ideality factor improved to 1.58 with passivation from 1.64 without passivation (PHPS = 0.02 vol%) (Fig. S12, ESI†),[48] suggesting that PHPS passivation reduces Shockley–Read–Hall recombination.

To further investigate the origin of the improved hole-extraction, the energy band diagram with and without passivation was analyzed by ultraviolet photoelectron spectroscopy (UPS) and angle-dependent hard X-ray photoelectron spectroscopy[49–51] (AD-HAXPES) (Fig. 5c). We measured the band shifting of the perovskite surface of the HTM side by using UPS and AD-HAXPES. ΔE is assigned to the difference between Fermi-level and valence band edge of the perovsktie. The changes of the ΔE is equivalent to the change in the charge concentration, which can be determined by the Fermi distribution and the state density function. After passivation (PHPS = 0.02 vol%), the Fermi-level of the perovskite surface was shifted to −4.68 eV from −4.56 eV as indicated in Fig. S13 and S14 (ESI†). Interestingly, we revealed that the ΔE of the perovskite was gradually shifted to the intrinsic-side with approaching the surface from the bulk (Fig. 5d and Fig. S15 (ESI†)). ΔE changes is due to the interaction of the lead with the silica passivation. It seems that the ΔE of the perovskite bulk was not influenced by PHPS treatment. In other words, in the case of samples with passivation, there was a noticeable ΔE changes between the surface and bulk Fermi-levels. Such ΔE changes can cause band-bending, which is a driving force for hole-extraction to the HTM (Fig. 5e). When the PHPS was oxidized, an ether bond can be generated between the substrate and the silica layer as $\langle Substrate{-}O^{2-}{-}Si^{4+}{-}\rangle$.[52] Thus, it probably can form the chemical bonding of $\langle Pb^{2+}{-}O^{2-}{-}Si^{4+}\rangle$ after the oxidation of the PHPS on the perovskite. This reaction is consistent with the XPS result of Pb shifting, which could be the reason for the band-bending. It was demonstrated that an interface change caused band bending in the depth direction of the perovskite layer for the first time to the best of our knowledge. Therefore, the PHPS derived
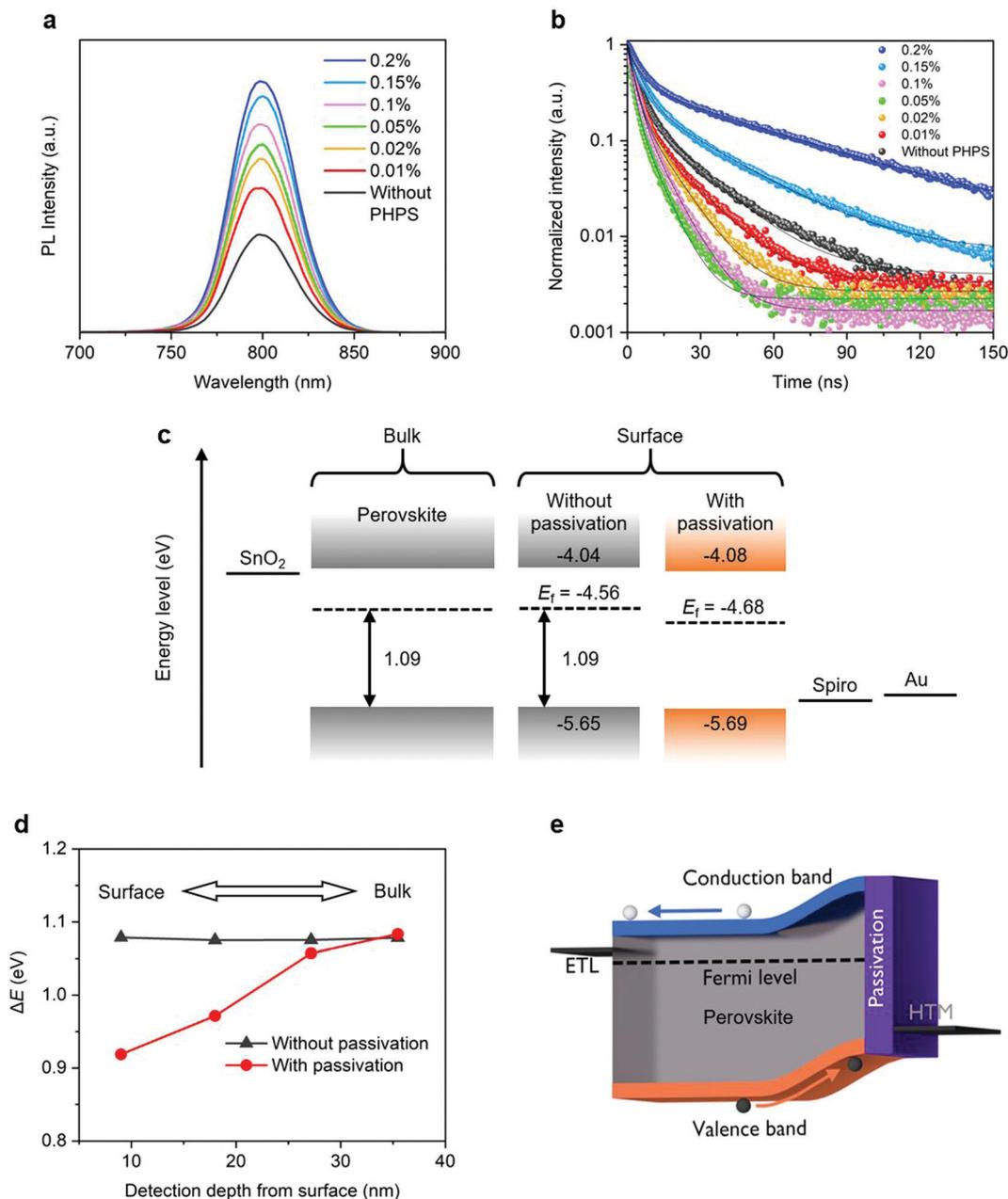
Fig. 5 Effect of perovskite surface passivation with PHPS treatment. Photoluminescence spectroscopy of (a) steady-state intensity and (b) decay as a function of PHPS solution concentration. (c) Energy band diagram of the perovskite with and without passivation. E_f is assigned to Fermi-Level. (d) ΔE as a function of the detection depth from perovskite surface. ΔE is assigned to the difference between Fermi-level and valence band edge. ΔE was changed from 0.92 eV at 9 nm to 1.08 eV at 35 nm. (e) Effect of band-bending induced passivation. The PHPS concentration is 0.02 vol% for the energy diagram.

passivation layer could serve to increase the V_{OC} and photo-conversion efficiency in perovskite solar cells.

To test how the inorganic passivation layer affected light stability, we measured the continuous performance of perovskite solar cells with and without passivation by maximum power point (MPP) tracking (Fig. 6). The performance dropped quickly at the initial time from 0 to 20 h. The reason for this quick performance drop could be cation migration, which would cause degradation of the perovskite and spiro-OMeTAD.[53] After 1000 h, we observed that the cells with passivation maintained 77% of

the initial efficiency, which was considerably higher than that for the cells without passivation (50% at 1000 h). In addition, the devices were stored in dry air and measured periodically. The passivated solar cell maintained 97% efficiency after 8000 h (Fig. S16, ESI†). These results indicate that applying inorganic passivation resulted not only in enhanced hole extraction from the bulk to the HTM but also in a more stable perovskite solar cell.

Finally, it was tested whether the protection layer using PHPS could also serve as a water repellant protection layer for
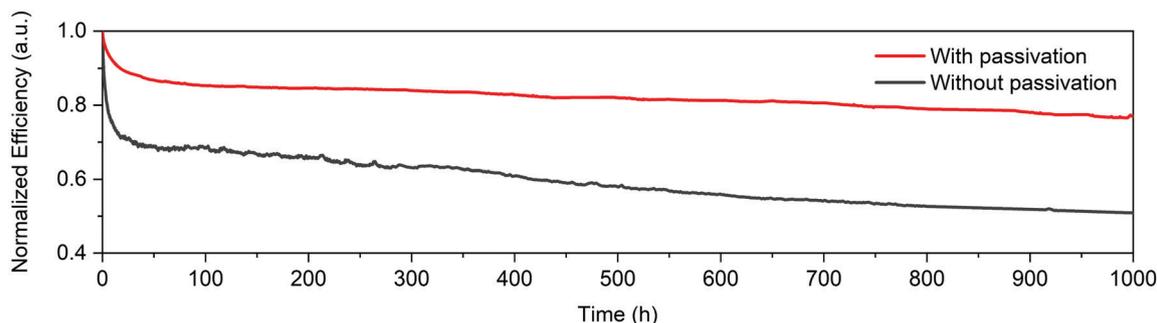
Fig. 6 Light stability of perovskite solar cells with and without passivation measured by maximum power point tracking. The PHPS concentration was 0.02 vol%.

perovskite solar cells (Fig. 7). To obtain the waterproofing effect, the device structure was changed from FTO/c-TiO$_2$/mp-TiO$_2$/c-SnO$_2$/perovskite/passivation layer/spiro-OMeTAD/Au (Fig. S17a, ESI†) to FTO/c-TiO$_2$/mp-TiO$_2$/c-SnO$_2$/perovsktie/spiro-OMeTAD/Au/thick protection layer (500 nm) (Fig. S17b, ESI†). The thick protection layer was deposited on the perovskite solar cell by spin-coating (3000 rpm, 20 vol%). Water (15 mL) was then dropped on the devices by spin-coating, and the efficiency of the solar cell was measured. Without the protection layer, dripping water on the device resulted in a 74% efficiency decrease and a marked difference in the solar cell appearance (Fig. 7b). However, the normalized efficiency of the devices with the protection layer was identical to the initial value (Fig. 7a and Table S2 (ESI†)). Furthermore, the perovskite layer was not degraded (Fig. 7b), as confirmed by X-ray diffraction (XRD) measurements (Fig. S18, ESI†). We reasoned, therefore, that the hydrophobic protection layer can also act as a water repellent (Fig. S19, ESI†). We also considered the waterproofing capability of the passivation layer at the perovskite/HTM interface. This structure was FTO/TiO$_2$/SnO$_2$/perovskite/PHPS/HTM/Au (Fig. S17a, ESI†) (the PHPS concentration was 0.02 vol%). The efficiency was decreased by 59.3%

(Fig. S20 and Table S3, ESI†), which was a result of the formed oxide layer being too thin to protect the perovskite layer.

Conclusions

We have demonstrated that PHPS derived silicon oxide can serve as an effective passivation layer for high-performance perovskite solar cells and elucidated the mechanism of the passivation. It was found that the passivation layer affect on the energy band of the perovskite surface by improving surface states. The changes in the energy level difference between the Fermi level and the valence band edge cause beneficial band-bending at the interface between the perovskite surface and the bulk, which acts as a driving force to enhance hole-extraction from the perovskite absorber layer. Consequently, the passivation design strategy we present here can improve the device V_{OC} to >1.1 V and the photoconversion efficiency to 22.13%. As an added benefit, the inorganic passivation layer can further improve the device stability compared with the non-treated cells, as well as behaving as remarkable waterproof protection when encapsulating perovskite solar cells.
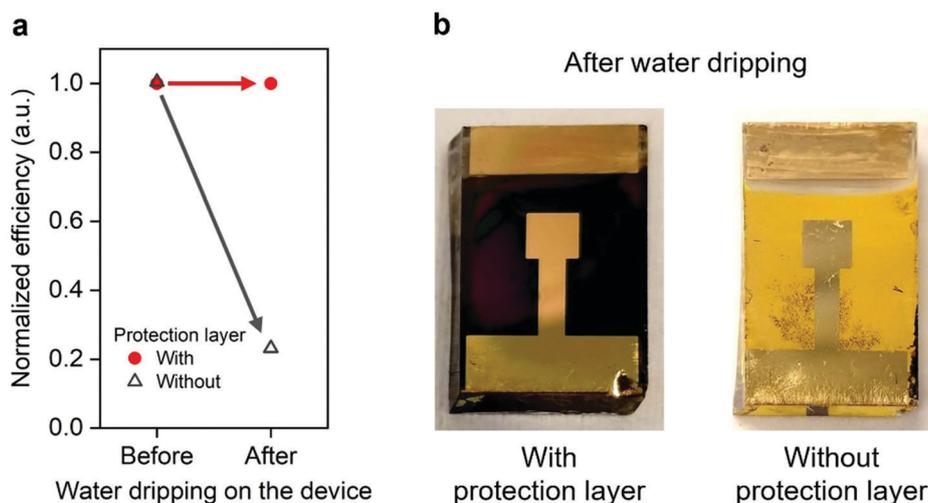
Fig. 7 Perovskite device waterproofing. (a) Normalized efficiency before and after water dripping on the device comparing with and without the protection layer using PHPS. Water was dropped on the device during spin-coating. (b) Device images after water dripping comparing with and without the protection layer. PHPS solution was deposited on the completed device. The PHPS concentration is 20 vol%.

Experimental

Materials

Perhydropolysilazane (PHPS, 20 vol%) was purchased from AZ Electronic Materials Co., Ltd. o-Xylene (99%, extra dry) was purchased from Fisher Scientific Inc. to dilute the PHPS. For fabrication of the perovskite layer, lead iodide and lead bromide were purchased from TCI Co. Ltd. Methylammonium bromide and formamidinium iodide were purchased from GreatCell Solar Ltd. Cesium iodide was obtained from abcr GmbH. All of the purchased chemicals were used as received without further purification. FTO glass (TEC-9AX) was purchased from NSG group. Titanium diisopropoxide bis(acetylacetonate) was purchased from Sigma-Aldrich. Titanium oxide nanoparticles (PST30NRD) were purchased from Great-Cell Solar. Tin chloride(IV) was purchased from Acros Organics. Bis(trifluoromethane)sulfonimide lithium salt and a cobalt-complex (FK209) were purchased from Sigma-Aldrich.

Device fabrication

A blocking TiO_2 layer was deposited on cleaned FTO glass by spray pyrolysis deposition of the precursor solution (1 mL of titanium diisopropoxide bis(acetylacetonate) in 15 mL ethanol) at 500 °C. Then, the mesoporous titanium oxide layer was deposited by spin-coating using a dispersed nanoparticle solution (1 g of titanium oxide nanoparticle paste in 11.8 g of ethanol) at 5000 rpm for 30 s, followed by annealing at 500 °C for 30 min. Subsequently, the tin-oxide layer was deposited by spin-coating with the precursor solution (0.1 M of tin chloride(IV) in deionized water) and annealed at 100 °C for 10 min and 190 °C for 1 h in air.[54] After that, UV/O_3 treatment (PSD series digital UV ozone system, Novascan Technologies, Inc.) was performed for 15 min. To form the perovskite layer, a perovskite precursor solution was prepared with a lead excess $(FAPbI_3)_{0.875}$-$(MAPbBr_3)_{0.125}(CsPbI_3)_{0.1}$ by mixing lead iodide (1.2 M), lead bromide (0.15 M), formamidinium iodide (1.0 M), methylammonium bromide (0.15 M), and cesium iodide (0.13 M) in DMF : DMSO = 4 : 1 (volume ratio). The perovskite solution was spun on the substrate with a two-step spin-coating program set at 2000 and 5000 rpm for 10 and 30 s, respectively. During spin-coating, 100 μL of chlorobenzene was dripped on the substrate 10 s before the termination time of the spin-coating. Then, the substrate was annealed at 100 °C for 1 h to crystallize the perovskite layer. After that, a solution of PHPS diluted in o-xylene (0.01–0.2 vol%) was spun on the substrate at 4000 rpm for 30 s followed by keeping in dry air (5% relative humidity) for 30 min. To deposit the hole-transport material (HTM), 80 mg of spiro-OMeTAD solution was diluted in 1023 μL of chlorobenzene, followed by adding 32 μL of 4-tert-butylpyridine, 19 μL of bis(trifluoromethane)sulfonimide lithium salt solution (517 mg mL^{-1}) in acetonitrile, and 14 μL of cobalt-complex solution (376 mg mL^{-1}) in acetonitrile. The prepared spiro-OMeTAD solution was spun on the substrate at 4000 rpm for 30 s. Last, a 70 nm Au layer was deposited on the HTM as a counter electrode.

Characterization and measurements

I–V measurements were performed using an Oriel VeraSol solar simulator (Newport Corporation) calibrated by an LCE-50 (Centronics). The I–V measurements were performed from 1.2 to 0 V as a reverse scan and from 0 to 1.2 V as a forward scan with a mask of 3×3 mm^2. The scanning step and speed were 10 mV and 50 mV s^{-1}, respectively. UV/vis spectroscopy was performed using a Lambda 950S (PerkinElmer, Inc.). Photoluminescence emission spectra were measured by using a LS-55 fluorescence spectrometer (PerkinElmer, Inc.). The conditions for the PL measurements were set as 610 nm for the excitation wavelength and a 10 nm emission slit. Time-resolved photoluminescence was measured using a time-correlated single photon counting system (Nanofinder 30). The wavelength for excitation was 480 nm. The wavelength for the detector was 791–797 nm. The morphology was assessed using a cold field emission scanning electron microscope (SU8200, Hitachi high-tech. Co.). One dimensional X-ray diffraction (XRD) analysis was carried out using a D8 Advance diffractometer (Bruker Corporation) with Cu Kα radiation ($\lambda_{K\alpha}$ = 1.5418 Å). Two-dimensional wide-angle X-ray scattering (2D-WAXS) patterns represented in reciprocal lattice space were conducted at Spring-8 on beamline BL19B2. The sample was irradiated with an X-ray energy of 12.39 keV (λ = 1 Å) at a fixed incident angle on the order of 6.0° through a Huber diffractometer. The 2D-WAXS patterns were recorded with a two-dimensional image detector (Pilatus 300 K). An ultraviolet photoelectron spectrometer (UPS) equipped with a He–I source ($h\nu$ = 21.22 eV) (AXIS Nova, Kratos Analytical Ltd, UK) was used to determine the valence band energy and Fermi-level. The Fermi-level of the samples was referenced to that of Au which was in electrical contact with a sample in UPS measurements. Angle-dependent hard X-ray photoemission spectroscopy (AD-HAXPES) at 7940 eV was performed using the Scienta R4000 system at the BL46XU beamline at SPring-8. The X-ray photoelectron spectroscopy (XPS) measurements were carried out on a VersaProbe II (Physical Electronics Inc.) with a monochromator and a source of Al-Kα 1486.6 eV. The spectrum was referenced using the C–C bound component of adventitious carbon. The stability test was performed as maximum power tracking under 100 mW cm^{-2} illumination with a LED power source, encapsulating samples in a measurement box purged with argon gas at 0% humidity kept at 25 °C by a cooling system.

Author contributions

H. K. conceived the idea and device fabrication and wrote the manuscript. N. S. assisted in writing the manuscript and performed 2D-WAXS and HAXPES experiments and analyzed the data. A. J. H., Y. L., S. P., N. K., C. R., V. L. E. Q., G. G., Y. Z., M. A., and K. T. C. assisted in device fabrication. M. D. M. and M. L. assisted in XPS measurement. M. K. N. supervised the project. All authors contributed to discussions and to finalizing the manuscript.

Conflicts of interest

There are no conflicts to declare.

Acknowledgements

References

1 N. J. Jeon, J. H. Noh, W. S. Yang, Y. C. Kim, S. Ryu, J. Seo and S. Il Seok, *Nature*, 2015, **517**, 476–480.

2 N. J. Jeon, H. Na, E. H. Jung, T. Y. Yang, Y. G. Lee, G. Kim, H. W. Shin, S. Il Seok, J. Lee and J. Seo, *Nat. Energy*, 2018, **3**, 682–689.

3 Q. Jiang, L. Zhang, H. Wang, X. Yang, J. Meng, H. Liu, Z. Yin, J. Wu, X. Zhang and J. You, *Nat. Energy*, 2016, **2**, 16177.

4 M. Wei, F. P. G. de Arquer, G. Walters, Z. Yang, L. N. Quan, Y. Kim, R. Sabatini, R. Quintero-Bermudez, L. Gao, J. Z. Fan, F. Fan, A. Gold-Parker, M. F. Toney and E. H. Sargent, *Nat. Energy*, 2019, **4**, 197–205.

5 H. Zhou, Q. Chen, G. Li, S. Luo, T. B. Song, H. S. Duan, Z. Hong, J. You, Y. Liu and Y. Yang, *Science*, 2014, **345**, 542–546.

6 A. Kojima, K. Teshima, Y. Shirai and T. Miyasaka, *J. Am. Chem. Soc.*, 2009, **131**, 6050–6051.

7 H.-S. Kim, C.-R. Lee, J.-H. Im, K.-B. Lee, T. Moehl, A. Marchioro, S.-J. Moon, R. Humphry-Baker, J.-H. Yum, J. E. Moser, M. Grätzel and N.-G. Park, *Sci. Rep.*, 2012, **2**, 591.

8 M. M. Lee, J. Teuscher, T. Miyasaka, T. N. Murakami and H. J. Snaith, *Science*, 2012, **338**, 643–647.

9 J.-H. Im, C.-R. Lee, J.-W. Lee, S.-W. Park and N.-G. Park, *Nanoscale*, 2011, **3**, 4088–4093.

10 Best Research-Cell Efficiencies (NREL, 2019), https://www. nrel.gov/pv/cell-efficiency.html.

11 Z. Chen, Q. Dong, Y. Liu, C. Bao, Y. Fang, Y. Lin, S. Tang, Q. Wang, X. Xiao, Y. Bai, Y. Deng and J. Huang, *Nat. Commun.*, 2017, **8**, 1890.

12 Q. Lin, A. Armin, R. C. R. Nagiri, P. L. Burn and P. Meredith, *Nat. Photonics*, 2015, **9**, 106–112.

13 C. Wehrenfennig, G. E. Eperon, M. B. Johnston, H. J. Snaith and L. M. Herz, *Adv. Mater.*, 2014, **26**, 1584–1589.

14 G. Xing, N. Mathews, S. Sun, S. S. Lim, Y. M. Lam, M. Grätzel, S. Mhaisalkar and T. C. Sum, *Science*, 2013, **342**, 344–347.

15 Q. Dong, Y. Fang, Y. Shao, J. Qiu, L. Cao and J. Huang, *Science*, 2015, **347**, 967–970.

16 S. D. Stranks, G. E. Eperon, G. Grancini, C. Menelaou, M. J. P. Alcocer, T. Leijtens, L. M. Herz, A. Petrozza and H. J. Snaith, *Science*, 2013, **342**, 341–344.

17 G. E. Eperon, S. D. Stranks, C. Menelaou, M. B. Johnston, L. M. Herz and H. J. Snaith, *Energy Environ. Sci.*, 2014, **7**, 982–988.

18 G. Xing, N. Mathews, S. S. Lim, N. Yantara, X. Liu, D. Sabba, M. Grätzel, S. Mhaisalkar and T. C. Sum, *Nat. Mater.*, 2014, **13**, 476–480.

19 H. Huang, J. Raith, S. V. Kershaw, S. Kalytchuk, O. Tomanec, L. Jing, A. S. Susha, R. Zboril and A. L. Rogach, *Nat. Commun.*, 2017, **8**, 996.

20 A. Polman, M. Knight, E. C. Garnett, B. Ehrler and W. C. Sinke, *Science*, 2016, **352**, aad4424.

21 W. Tress, *Adv. Energy Mater.*, 2017, **7**, 1602358.

22 W. Shockley and H. J. Queisser, *J. Appl. Phys.*, 1961, **32**, 510–519.

23 N. K. Noel, S. N. Habisreutinger, A. Pellaroque, F. Pulvirenti, B. Wenger, F. Zhang, Y.-H. Lin, O. G. Reid, J. Leisen, Y. Zhang, S. Barlow, S. R. Marder, A. Kahn, H. J. Snaith, C. B. Arnold and B. P. Rand, *Energy Environ. Sci.*, 2019, **12**, 3063–3073.

24 D. Bi, C. Yi, J. Luo, J.-D. Décoppet, F. Zhang, S. M. Zakeeruddin, X. Li, A. Hagfeldt and M. Grätzel, *Nat. Energy*, 2016, **1**, 16142.

25 L. Zuo, H. Guo, D. W. de Quilettes, S. Jariwala, N. De Marco, S. Dong, R. De Block, D. S. Ginger, B. Dunn, M. Wang and Y. Yang, *Sci. Adv.*, 2017, **3**, e1700106.

26 B. Chaudhary, A. Kulkarni, A. K. Jena, M. Ikegami, Y. Udagawa, H. Kunugita, K. Ema and T. Miyasaka, *ChemSusChem*, 2017, **10**, 2473–2479.

27 Q. Jiang, Y. Zhao, X. Zhang, X. Yang, Y. Chen, Z. Chu, Q. Ye, X. Li, Z. Yin and J. You, *Nat. Photonics*, 2019, **13**, 460–466.

28 E. H. Jung, N. J. Jeon, E. Y. Park, C. S. Moon, T. J. Shin, T.-Y. Yang, J. H. Noh and J. Seo, *Nature*, 2019, **567**, 511–515.

29 X. Zheng, B. Chen, J. Dai, Y. Fang, Y. Bai, Y. Lin, H. Wei, X. C. Zeng and J. Huang, *Nat. Energy*, 2017, **2**, 17102.

30 N. K. Noel, B. Wenger, S. N. Habisreutinger, J. B. Patel, T. Crothers, Z. Wang, R. J. Nicholas, M. B. Johnston, L. M. Herz and H. J. Snaith, *ACS Energy Lett.*, 2018, **3**, 1233–1240.

31 H. Tan, A. Jain, O. Voznyy, X. Lan, F. P. G. De Arquer, J. Z. Fan, R. Quintero-Bermudez, M. Yuan, B. Zhang, Y. Zhao, F. Fan, P. Li, L. N. Quan, Y. Zhao, Z. H. Lu, Z. Yang, S. Hoogland and E. H. Sargent, *Science*, 2017, **355**, 722–726.

32 Z. Zhang and J. T. Yates, *Chem. Rev.*, 2012, **112**, 5520–5551.

33 A. D. Mallorquí, E. Alarcón-Lladó, I. C. Mundet, A. Kiani, B. Demaurex, S. De Wolf, A. Menzel, M. Zacharias and A. Fontcuberta i Morral, *Nano Res.*, 2014, **8**, 673–681.

34 M. Mews, M. Liebhaber, B. Rech and L. Korte, *Appl. Phys. Lett.*, 2015, **107**, 013902.

35 M. Çopuroğlu, H. Sezen, R. L. Opila and S. Suzer, *ACS Appl. Mater. Interfaces*, 2013, **5**, 5875–5881.

36 R. Varache, J. P. Kleider, W. Favre and L. Korte, *J. Appl. Phys.*, 2012, **112**, 123717.

37 Z. Zhang, Z. Shao, Y. Luo, P. An, M. Zhang and C. Xu, *Polym. Int.*, 2015, **64**, 971–978.

38 Y. N. Sun, A. Feldman and E. N. Farabaugh, *Thin Solid Films*, 1988, **157**, 351–360.

39 S. Naskar, S. D. Wolter, C. A. Bower, B. R. Stoner and J. T. Glass, *Appl. Phys. Lett.*, 2005, **87**, 261907.

40 J. Yang, Q. Hong, Z. Yuan, R. Xu, X. Guo, S. Xiong, X. Liu, S. Braun, Y. Li, J. Tang, C. Duan, M. Fahlman and Q. Bao, *Adv. Opt. Mater.*, 2018, **6**, 1800262.

41 T. Kim, S. Koka, S. Surthi and K. Zhuang, *IEEE Electron Device Lett.*, 2013, **34**, 405–407.

42 M. Saliba, T. Matsui, J.-Y. Seo, K. Domanski, J.-P. Correa-Baena, M. K. Nazeeruddin, S. M. Zakeeruddin, W. Tress, A. Abate, A. Hagfeldt and M. Grätzel, *Energy Environ. Sci.*, 2016, **9**, 1989–1997.

43 L.-Q. Xie, L. Chen, Z.-A. Nan, H.-X. Lin, T. Wang, D.-P. Zhan, J.-W. Yan, B.-W. Mao and Z.-Q. Tian, *J. Am. Chem. Soc.*, 2017, **139**, 3320–3323.

44 H. Tsai, R. Asadpour, J.-C. Blancon, C. C. Stoumpos, O. Durand, J. W. Strzalka, B. Chen, R. Verduzco, P. M. Ajayan, S. Tretiak, J. Even, M. A. Alam, M. G. Kanatzidis, W. Nie and A. D. Mohite, *Science*, 2018, **360**, 67–70.

45 R. S. Bonilla and P. R. Wilshaw, *J. Appl. Phys.*, 2017, **121**, 135301.

46 M. Garín, U. Rau, W. Brendle, I. Martín and R. Alcubilla, *J. Appl. Phys.*, 2005, **98**, 093711.

47 C. M. Wolff, F. Zu, A. Paulke, L. P. Toro, N. Koch and D. Neher, *Adv. Mater.*, 2017, **29**, 1700159.

48 N. Shibayama, H. Kanda, T. W. Kim, H. Segawa and S. Ito, *APL Mater.*, 2019, **7**, 031117.

49 S. Tanuma, C. J. Powell and D. R. Penn, *Surf. Interface Anal.*, 1994, **21**, 165–176.

50 B. Philippe, T. J. Jacobsson, J.-P. Correa-Baena, N. K. Jena, A. Banerjee, S. Chakraborty, U. B. Cappel, R. Ahuja, A. Hagfeldt, M. Odelius and H. Rensmo, *J. Phys. Chem. C*, 2017, **121**, 26655–26666.

51 B. Philippe, M. Saliba, J.-P. Correa-Baena, U. B. Cappel, S.-H. Turren-Cruz, M. Grätzel, A. Hagfeldt and H. Rensmo, *Chem. Mater.*, 2017, **29**, 3589–3596.

52 J. Song, D. Wang, L. Hu, X. Huang and Y. Chen, *Appl. Surf. Sci.*, 2018, **455**, 771–779.

53 Q. Li, Y. Zhao, R. Fu, W. Zhou, Y. Zhao, F. Lin, S. Liu, D. Yu and Q. Zhao, *J. Mater. Chem. A*, 2017, **5**, 14881–14886.

54 Y. Lee, S. Paek, K. T. Cho, E. Oveisi, P. Gao, S. Lee, J.-S. Park, Y. Zhang, R. Humphry-Baker, A. M. Asiri and M. K. Nazeeruddin, *J. Mater. Chem. A*, 2017, **5**, 12729–12734.